



RESEARCH ARTICLE

10.1002/2017JA024214

Characterization of Jupiter's secondary auroral oval and its response to hot plasma injections

Key Points:

- During January 2014 Jupiter's UV aurora exhibits a lower latitude second oval feature
- The magnetospheric source region lies around 9–13 R_J and close to hot plasma injections
- Wave-particle interactions may enhance the oval brightness 1–3 days after the hot plasma injections

Correspondence to:

R. L. Gray,
r.gray@lancaster.ac.uk

Citation:

Gray, R. L., S. V. Badman, E. E. Woodfield, and C. Tao (2017), Characterization of Jupiter's secondary auroral oval and its response to hot plasma injections, *J. Geophys. Res. Space Physics*, 122, 6415–6429, doi:10.1002/2017JA024214.

Received 10 APR 2017

Accepted 9 JUN 2017

Accepted article online 14 JUN 2017

Published online 28 JUN 2017

R. L. Gray¹ , S. V. Badman¹ , E. E. Woodfield² , and C. Tao³

¹Department of Physics, Lancaster University, Lancaster, UK, ²British Antarctic Survey, Cambridge, UK, ³National Institute of Information and Communications Technology, Tokyo, Japan

Abstract We present Jovian auroral observations from the 2014 January Hubble Space Telescope (HST) campaign and characterize the auroral second oval feature with particular attention to the response to hot plasma injections. The location of the second oval feature lies between the Ganymede and Europa moon footprint contours between 150 and 240° system III longitude, corresponding to a source in the inner magnetosphere between 9 and 13 R_J . At the examined longitudes, this is in the same region of 11–16 R_J known as the pitch angle distribution boundary, beyond which electrons are thought to be scattered into a field-aligned configuration and cause auroral precipitation. The feature is enhanced in both brightness and longitudinal spread 1–3 days after large hot plasma injections. The precipitating electrons have a higher-energy and lower flux than the electrons generating large injection signatures. We suggest that wave-particle interactions are responsible for the scattering of electrons in this region. We also suggest that the plasma injections can act as a temperature anisotropy and particle source to enhance electron scattering into the aurora and the brightness of the second oval feature. Changes to the magnetic field topology around an injection may also generate shear Alfvén waves and therefore accelerate electrons parallel to the magnetic field resulting in precipitation.

1. Introduction

Jupiter's aurora is typically divided into three morphological categories based on their position relative to the main auroral emission, also known as the main auroral oval; the polar emissions, the main emission itself, and the outer emissions. The main emission is generated by upward currents from the “plasma corotation breakdown region” in the middle magnetosphere (15–40 R_J) [Hill, 2001; Cowley and Bunce, 2001; Vogt et al., 2011]. Auroral signatures that appear equatorward of the main emission correspond to currents generated planetward of the plasma corotation breakdown region in the magnetosphere. These “outer emissions” have three main forms. These are the moon footprints, the injection signatures, and the second oval.

The moon footprints are the most equatorward emissions [Bonfond, 2012]. They are used to validate mapping along magnetic field lines between magnetospheric source regions and the ionospheric auroral signatures, because their location in the magnetosphere is known.

Diffuse equatorward emissions have been linked to injections of hot plasma, which have been detected at 9–27 R_J radial distance, extending up to 1 R_J in azimuth [Mauk et al., 1999, 2002]. There are probably two plasma sources of injection signatures. These are plasma outflow, which triggers interchange, and possibly plasma inflows associated with tail reconnection. Interchange can be driven by Io plasma torus (IPT) outflow; hot, tenuous and cold, dense plasma interchanges position in order to conserve magnetic flux. Narrow interchange fingers have been detected in the vicinity of Io [Kivelson et al., 1997; Thorne et al., 1997].

Interchange may also be expected in the middle magnetosphere as hot inflows from reconnection encounter the colder, denser plasma in the middle magnetosphere. The connection between hot tail inflows and injections has been demonstrated using radio emissions by Louarn et al. [2014], who found that “reconfiguration events” (reconnection events in the tail) occurred within 10 h of “energetic events” (particle injection events in the inner magnetosphere). Gray et al. [2016] analyzed auroral images from the 2014 Hubble Space Telescope (HST) campaign and inferred that hot inflows from reconnection were associated with injections in the inner magnetosphere. They presented observations of a superrotating polar spot passing into a large feature where the main emission would be expected, and in the presence of large injection signatures. They postulated that the main emission feature was indicative of a boundary region in the middle magnetosphere between

©2017. The Authors.

This is an open access article under the terms of the Creative Commons Attribution License, which permits use, distribution and reproduction in any medium, provided the original work is properly cited.

a prolonged interval of hot inflows from the tail and consequential hot plasma injections in the inner magnetosphere.

Auroral injection signatures have been typically identified as a few degree wide “blobs” [Mauk *et al.*, 2002; Bonfond *et al.*, 2012; Dumont *et al.*, 2014; Gray *et al.*, 2016]. It is thought that the larger injection signatures could be composed of smaller injections, showing substructure similar that found in Galileo Energetic Particles Detector (EPD) measurements [Mauk *et al.*, 1997]. Radioti *et al.* [2013] showed simultaneous energetic neutral atom and auroral observations at Saturn of injection signatures evolving into several small signatures. The injection features can be driven either by scattering of electrons into the loss cone or by field-aligned currents associated with pressure gradients within and at the boundaries of the hot plasma.

Wave-particle interactions in the region 10–17 R_J are thought to scatter electrons into a field-aligned distribution, leading to a transition region at these distances where the electron pitch angle distribution (PAD) changes and to a second auroral oval sometimes visible at lower latitudes than the main oval [Bhattacharya *et al.*, 2001; Grodent *et al.*, 2003; Tomás *et al.*, 2004a, 2004b; Radioti *et al.*, 2009]. This feature tends to be less bright than the injection signatures, appearing in sections of discrete arcs of varying length.

Hot plasma injections in the PAD transition region may be expected to act as a particle source and source of energy for wave growth for wave-particle interactions and therefore increase scattering into the ionosphere [Xiao *et al.*, 2003], causing the second oval to become more visible. This paper quantifies the location and intensification of the second oval feature in response to the occurrence of hot plasma injections.

2. Observation Overview and Data Reduction

The Hubble Space Telescope (HST) Space Telescope Imaging Spectrograph (STIS) with the SrF2 filter was used to capture “time tag” images of Jupiter’s FUV northern aurora between days of year 001 to 016 of 2014. These emissions mainly consist of H Lyman alpha and H₂ Lyman and Werner bands. The band pass of the SrF2 filter is 1250–1900 Å, i.e., it rejects light at shorter wavelengths including the H Lyman alpha line at 1215 Å. There is on average one HST “visit” per day, with exceptions of day 011 and day 013 having two and three visits respectively. Each ~45 min long visit consists of two 700 s long time tag imaging observations interrupted by a 200 s spectral observation. The imaging observations are split into seven images with 100 s exposures.

The images were processed through the Boston University pipeline [Nichols *et al.*, 2009; Clarke *et al.*, 2009], correcting for dark current, flat field, and geometric distortion. The counts were converted to kilorayleighs emitted from H₂ over the wavelength range 700–1800 Å, assuming a color ratio of 2.5 [Gustin *et al.*, 2012]. The images were projected onto a planetocentric longitude-latitude grid on the surface of an oblate spheroid assuming a peak auroral emission height of 240 km above the 1 bar pressure level [Vasavada *et al.*, 1999]. The resolution of the projected image is 0.25° × 0.25°. Further details about data reduction and projection accuracy can be found in Nichols *et al.* [2009] and Grodent *et al.* [2003], respectively.

Figure 1 gives examples of the relevant morphologies observed. There is an injection signature on day 4, appearing outside the main oval (a). On days 5 (not pictured), 6 (Figure 1b), and 7 (Figure 1c), the second oval appears in bright arcs with diffuse emission between sections. After another injection event on day 11 (Figure 1d), a fuller second oval is seen on day 13 (Figure 1e). A further injection event on day 14 is indicated by a hectometric (HOM) radio emission at 20:00 UT, which has previously been linked to large reconfiguration events and injection events [Louarn *et al.*, 2014; Gray *et al.*, 2016]. On day 16 (Figure 1f), the fullest second oval is observed.

Three large injection events are detected through the 2014 HST campaign on days 4, 11, and 14 using the Hisaki instrument. In all three cases, Hisaki measurements show sudden transient increase in auroral power, indicating a reconfiguration and injection events [Kimura *et al.*, 2015]. On days 4 and 11, HST images show large auroral injection signatures (see Figures 1a and 1d). On day 14, a large HOM emission is observed. To analyze the response of the second oval feature to the injections, the campaign was split into two groups: observations which were within 3 days after an injection event (days 5, 6, 7, 11, 13, and 16) and the other observations (days 1, 2, 3, 4, and 10).

3. Feature Detection Algorithm

An automated detection algorithm was used to select the second oval points. The average position of the main emission over the campaign was found as follows: the average campaign image was binned into 1° system

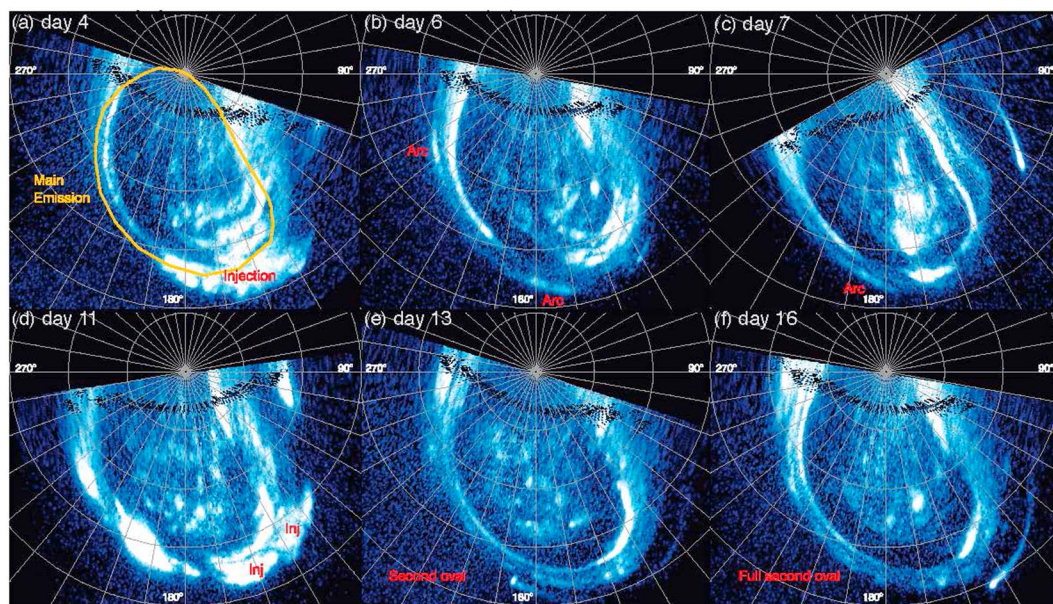


Figure 1. Six polar projected images taken with the HST, with log intensity scale saturated at 400 kR. For each image the exposure time was 100 s. The gray lines indicate a $10^\circ \times 10^\circ$ jovicentric latitude system III longitude grid. The image is oriented such that 180° system III longitude is directed toward the bottom and labels are displayed in gray. (a) Injection event, day 4 01:10 UT, average main emission position for campaign in gold, (b) day 6 02:35 UT, (c) day 7 07:16 UT. (d) Injection event, day 11 00:31 UT, (e) day 13 22:39 UT, and (f) after HOM emission on day 14, day 16 00:03 UT.

III longitude bins. The maximal brightness was found in each bin with the caveat that the latitude of maximal brightness was not to change more than 2° between adjacent longitude bins. This confines the brightness of the main emission to a strip a few degrees in latitude. The average main emission position for the campaign is shown in black crosses on Figure 2. For each visit, slices perpendicular to the main emission were taken at $\sim 0.25^\circ$ intervals. First, the main emission position along the slice was found. The outer bound of the slice is set as the footpoint of the field line that crosses the equatorial plane at $9 R_J$ (mapped with the VIPAL model *Hess et al., 2011*); the inner bound is 0.5° poleward of the average main emission position. A Gaussian is fit along the intensity profile of the slice (on the assumption that the main emission is bright and confined). The peak position of the Gaussian is taken as the main emission peak position for that slice if it is above 200 kR (to avoid selecting bright second oval peaks). The position of the main emission for the visit was found by averaging the points' positions in 20° spatial bins in longitude around the central point at 175° longitude, 66° latitude (which was empirically determined).

The second peaks were then found as follows: an average main emission position is found for each visit by incrementally expanding the average main emission shape from 0.25° of its original shape till it best fits the main emission points found for that visit. This maintains the expected shape of the main emission for regions where the emission is dim on that visit. To define the latitudinal "slice" at each location, the inner bound of the intensity profile along the slice is 0.5° equatorward of the adjusted average main emission position and the outer bound was the footprint of the field line that crosses the equatorial plane at $7 R_J$, (just outside the orbit of Io). These boundaries are shown in Figure 2.

The brightness profile across the slices were examined. Examples of these profiles are shown in Figure 3. It was assumed that in the absence of a second oval peak, the intensity falls exponentially from the main emission, so each intensity slice had a fitted Gaussian background across the slice removed (blue, Figure 3, top), with intensity values below the Gaussian set to zero. The peak of the remaining intensities (red) was selected as the second oval point. If a Gaussian with a peak greater than a threshold of 200 kR could not be fitted (i.e., the main emission is dim), then the greatest peak outside the adjusted average main emission was selected as the second oval point (Figure 3, bottom). Second oval points with brightness below 40 kR and above 400 kR were rejected—these are too dim or bright to constitute a typical second oval feature. Points greater than 400 kR are typical of injection signatures or main emission brightness. The longitude, latitude, and peak brightness of each point was measured for each slice per visit. This was repeated for each slice per visit.

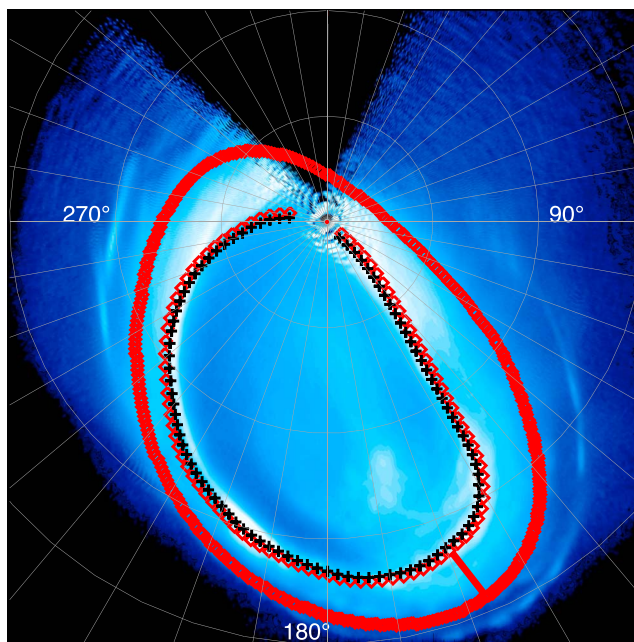


Figure 2. Polar projected HST UV 2014 campaign average image with inner and outer boundaries of intensity slices (red diamonds) used for second peak detection. Inner boundary is an example adjusted main emission; outer emission is the footpoint of the field line that crosses the equatorial plane at $7 R_J$ mapped with the VIPAL model. For peak detections, slices are taken between pairs of points. Average main emission also shown (black crosses). An example slice is shown around 160° longitude in red.

The points were then refined based on a derived average position as follows. The peaks detected were binned into 20° longitude bins (as for the main emission point selection) and an average second emission position for the visit was found. Data points which lay more than 1° away from this derived average position or within 1° latitude of the adjusted main emission were rejected so that a dim and broad main emission point would not be mistakenly selected as a second oval point. After this refinement, the longitude, latitude, and peak brightness of each point was measured again. This was repeated for each visit.

The moon footprints of Ganymede and Europa can appear in the region of interest, and their effects are twofold. First, the moon footprints themselves will contribute to the brightness profiles. Second, it is thought that the moons may be able to cause enhanced pitch angle scattering of particles as they pass through a region [Santolik *et al.*, 2011]. Points that lie either 1° ahead or 4° behind in longitude and within 1° latitude of the projected position of the Europa and Ganymede moon footprints (found by matching the moon phase to the footprint contour in Hess *et al.* [2011]) have been removed.

Only points found between longitudes 150° – 240° were investigated. Longitudes greater than 240° were not accessed in many visits due to the viewing geometry or tend to be observed close the planetary limb so may appear artificially brightened. At longitudes less than 150° , the equatorward diffuse emission (EDE) region reported in Radioti *et al.* [2009] is prominent. The EDE region appears broad in latitude and has a low brightness. This is not the type of morphology that the program is designed to select, although the generation mechanism is likely related to that of the second oval. Points found on images with large injection signatures (days 4 and 11), expanded and disjointed emission (day 2), or with exceptionally poor viewing geometry (visit 2 on day 13) are rejected.

To find the average second emission location for the whole campaign, all accepted points were binned into 10° longitude bins and the average position and brightness were found.

4. Results

4.1. Second Oval Location

Figure 4 shows two example outputs for days 6 (a) and 16 (b) overlaid with points where second oval points are detected. The images are averaged over the visit. Figure 4c shows both sets of points overlaid with the

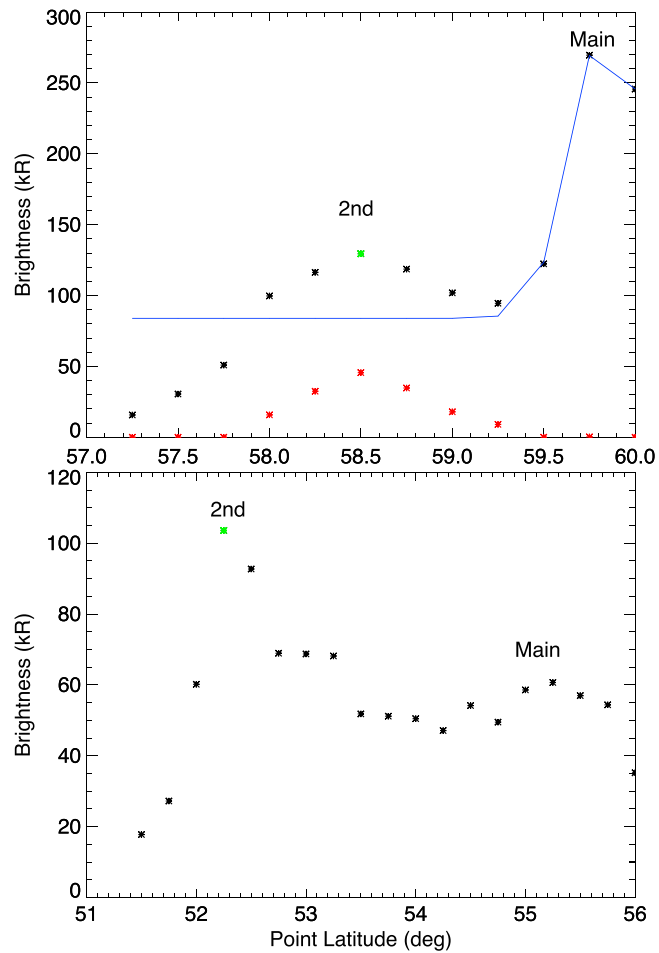


Figure 3. Two example intensity profiles from day 16 showing the second oval point selected (green). (top) The 148° longitude, clear main and second oval peaks; Gaussian profile (blue) subtracted from intensities (black) to give residual emission (red). (bottom) The 160° longitude, clear second but dim main emission; highest peak selected.

campaign average main emission in gold to guide the eye. Green points are from day 6 and red points are from day 16. Day 6 shows two clear bright arcs, the 150 kR contours of which extend to 220–242° longitude and 66–71° latitude and 170–182° longitude and 53–55° latitude, respectively. The automated detection has picked out these points as well as a fainter arc between the two. The three right most points from day 6 (Figure 4a) are examples of the detection failing to select the second oval and selecting either diffuse emission

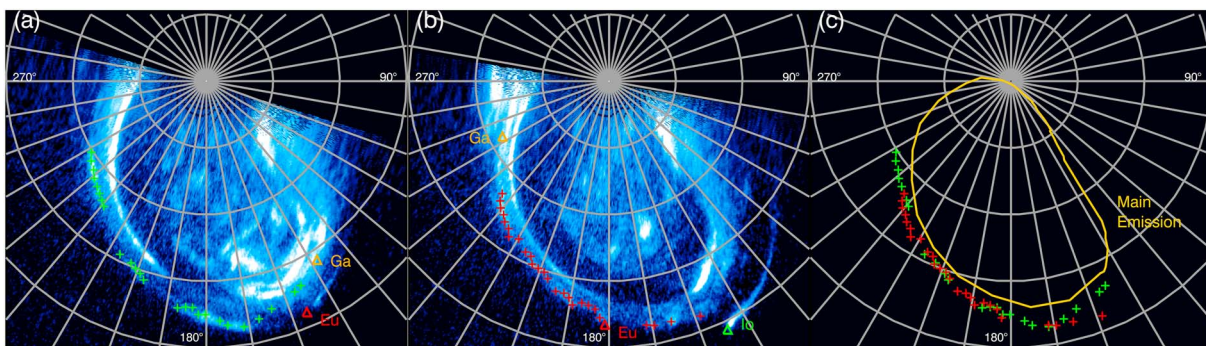


Figure 4. Two HST images from (a) day 6 and (b) day 16 with overplotted selected second oval points. (c) Second oval points from both day 6 (green) and day 16 (red), with the campaign average main emission to guide the eye. Moon footprint positions are also overplotted.

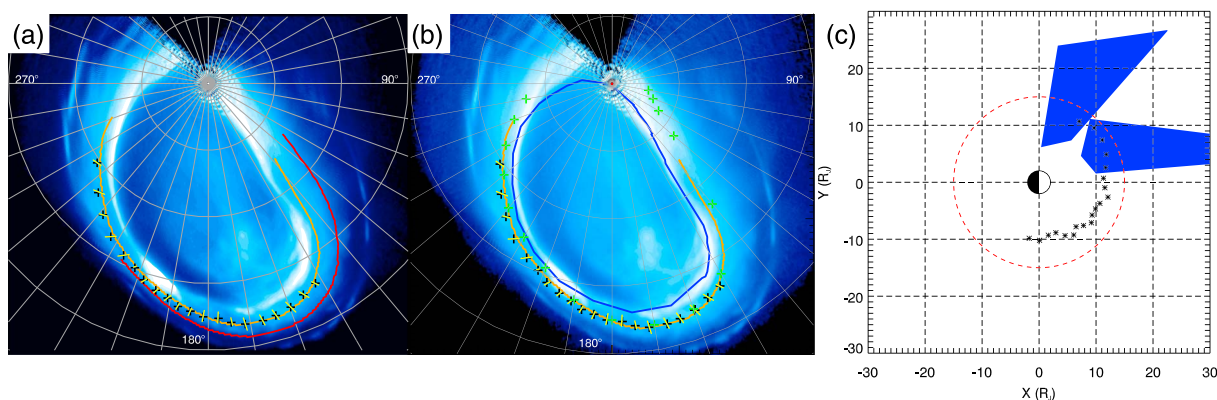


Figure 5. (a) Average campaign emission image with overplotted moon footprint contours (Europa in red, Ganymede in orange) and second oval points (black) with errors (yellow) of ± 1 standard deviation either side. (b) Average campaign image with average main emission (blue), second oval position (black) with error bars (yellow), the Ganymede footprint contour (orange), and previous second oval points from [Tomás et al., 2004b] (green). (c) The location in the equatorial plane of the auroral second oval (black) detected between 150 and 240° (in the ionosphere), and injections signatures (shaded blue) observed on 11 January 2014 (their position is consistent with, e.g., Louarn et al. [2014]). The red circle shows the $15 R_J$ line, which is the approximate orbital path of Ganymede. The VIPAL internal field model was used to map the features [Hess et al., 2011] with a CAN current sheet [Connerney et al., 1981]. The positive x axis points to the Sun, and the mapping is performed for 180° central meridian longitude.

or the edge of the disjointed main emission instead—the points form less of an arc and therefore do not constitute the second oval. The brighter features of the oval on day 16 have also been detected.

Figure 5a shows the mean average campaign image with the position of the second oval and the Ganymede (orange) and Europa (red) footprint contours, detected between 150 and 240° longitude [Hess et al., 2011]. The average position falls close to the Ganymede footprint and tends to be between the Ganymede and Europa footprints. The moon footprint flux tubes in the equatorial plane lie at the moon, so the statistical position of the flux tubes forming the second emission in the equatorial plane lies between the two moon orbital paths, i.e., between $9.5 R_J$ (Europa) and $15 R_J$ (Ganymede). Yellow error bars indicate ± 1 standard deviation on either side of the mean in each bin—they point toward the center used for finding the average binned second oval location. The points are confined to an oval that is narrow in latitude and spread across all longitudes sampled by the detection algorithm. The average ionospheric longitude and latitude can be found in Table 1.

HST images taken on days 5, 6, and 7 (Figure 1) show evolution following an injection event on day 4. There are three arcs of emission constrained in latitude centered around 230° , 200° , and 180° longitude on day 6. Figure 4 shows the points identified by the algorithm on days 6 and 16 superimposed on the HST images. As mentioned above, the rightmost detected points from day 6 (green) should be ignored since they are not the second oval emission but correspond to the edge of the broader and more diffuse main emission. The arc features (green) of day 6 lie along the same line of ‘full’ oval points (red) taken from day 16.

Previous work by Tomás et al. [2004a, 2004b] and Tomás [2005] has linked the second oval appearance to the PAD boundary in the vicinity 10 – $17 R_J$. The PAD boundary is thought to be a consequence of the Nishida recirculation process whereby energetic particles radially diffuse inward in the equatorial plane, pitch angle scatter in the inner magnetosphere, latitudinally diffuse at low altitudes to larger L shells, and are so recirculated to radially distant regions [Nishida, 1976; Fujimoto and Nishida, 1990]. Wave-particle interactions (pitch angle scattering) in the region 10 – $17 R_J$ (the inner magnetosphere) are thought to scatter electrons into a field-aligned distribution, leading to auroral precipitation and to a second auroral oval. Figure 5b shows the position of the previously reported second oval (green) [after Tomás, 2005] compared to the second oval (black with yellow error bars) detected in this work from the 2014 HST campaign. Points found in this work closely follow the Ganymede footprint contour, corresponding to a source close to the Ganymede orbital path (at around $15 R_J$). The previous work shows that the second oval (green) lies slightly poleward of the second oval points and errors found in this current work around 200 – 210° longitude. This corresponds to a source that is farther from the planet than that of the current work. In Grodent et al. [2003], it is suggested that the second oval emissions merge with the main emission around 205° longitude; we found that the two emissions do not merge but stay separated over 150 – 240° in the January 2014 events.

Table 1. System III Longitude and Latitude of Mean Second Emission

Ionospheric Longitude (°)	Ionospheric Latitude (°)	Equatorial Radial Distance (R_J)	Equatorial Longitude (°)
152.00	56.00	12.8	123.4
156.25	55.00	13.6	135.4
160.00	54.25	13.4	146.3
164.00	53.75	12.9	157.5
167.75	53.50	12.1	167.6
171.25	53.50	11.5	176.4
174.75	54.00	11.7	184.7
178.00	54.75	12.5	192.2
181.25	55.00	11.5	199.2
184.25	55.50	11.1	205.3
187.50	56.25	11.1	211.8
190.50	57.25	11.7	217.8
194.25	58.00	11.0	224.3
198.00	58.75	10.2	230.3
201.50	60.25	11.1	236.7
206.50	61.50	10.5	244.0
212.50	62.75	9.4	251.6
218.75	64.75	9.5	260.1
225.50	67.25	10.2	269.5
234.75	69.75	10.0	280.0

4.2. Magnetic Mapping of Features to Equatorial Plane

In order to investigate the potential magnetospheric source region of the auroral features, the field lines are mapped from the northern hemisphere to the equatorial magnetosphere using the VIPAL model. The VIPAL model [Hess *et al.*, 2011] is an update to the VIP4 internal magnetic field model and is based on Voyager and Pioneer magnetic field measurements, modeling of the lowest orders of the magnetic anomaly and corrects for the longitudinal position of the magnetic field lines mapping to Io's orbit. The points lie close to the Ganymede footprint contour, corresponding to a source around $15 R_J$ where the magnetic field begins transitioning from a more dipolar to a stretched configuration due to plasma sheet stretching. Therefore, the Connerney Acuña Ness (CAN) current sheet model is used in the mapping [Connerney *et al.*, 1981]. (Models of the magnetic field are presently not totally accurate and tend to map features closer to the planet—the mapping is used to give an indication of source region only. It is more meaningful to compare the position of the auroral feature to moon footprints as a validation of the map.)

Figure 5c shows the mapped location of the average second oval position calculated from the automated detection program (black) taken between 150 and 240° , the injection signatures from day 11 (blue), and the $15 R_J$ contour (red), roughly collocated with the orbit of the moon Ganymede. The mapped radial distance and equatorial longitudes can be found in table 1.

According to this mapping, the radial position of the second oval source varies between 9.4 and $13.6 R_J$, consistent with the auroral location between the Ganymede and Europa footprint contours as shown on Figure 5a. It has been detected in the region 123 – 279° system III longitude. The injections lie between 8.8 – $55.7 R_J$ and 6.3 – $34.9 R_J$ and around 129 – 174° and 94 – 130° system III longitude respectively, consistent with, e.g., Louarn *et al.* [2014]. The location of the second oval points lies within the edges of the mapped injection feature.

4.3. Auroral Brightness

Figure 6 shows a histogram of the brightness of the second oval feature through the 2014 campaign for the observations 3 days after injection events (red solid) and other observations (blue outline). A 3 day interval was chosen because the brightness increases for observations 3 days after injection events. The average brightness for all the second oval points is 133 ± 62 kR. For points after injection events, the mean brightness is 139 ± 65 kR; for other observations, the mean brightness is 112 ± 44 kR. There are six observations before injection events and eight after. More second oval points are detected during “postinjection” visits. There are

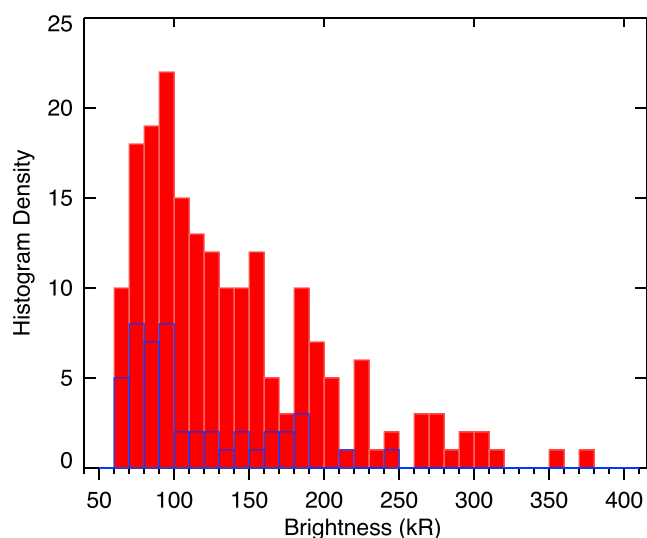


Figure 6. Histogram of brightness of second oval points for periods 3 days after an injection (red solid) and other days (blue outline).

over twice the number of points selected per bin around the modal brightness during postinjection visits. There is a larger tail for the postinjection visits, demonstrating that the second oval points selected are higher intensity.

Figure 7a shows the number of second oval points detected normalized to correct for variable viewing geometry caused by the auroral region moving in and out of view as the planet rotates. There are more points detected after an injection event than before it, indicating that the second oval is more enhanced after an injection event. In response to the day 4 injection, the number of second oval points detected increases from 12 (out of a possible maximum across all images of 80) to 29 on day 5, a slight decrease to 25 on day 6 and up to 35 on day 7. For the case of the day 11 injection event, Figure 7a shows that the increase in number of second oval points detected is from 11 on day 10 up to 27 on the last observation of day 13. For the day 14 injection event, the number increases further to 29. In general, then, there is an increase in the number of second oval points detected after injection events.

Superposed epoch analysis allows comparison of the responses of the second oval feature to injection events. The time of each injection event (taken as the first image where the events were detected for days 4 and 11, and with the HOM onset for day 14) is set to $t = 0$ days. Figure 7b shows the range of brightness of detected second oval points up to 4 days after the injection events.

It is noted that the mean brightness of the visits all lie within 1 standard deviation of each other. Following the first injection event, shown in red, the mean brightness of the detected second oval points begins at 143 kR on day 5, peaks at 171 kR on day 6, and falls to 123 kR on day 7. Despite the decrease in number of points detected on day 6 (Figure 7a), the brightness of the points is higher than that of day 7. It is suggested that there are more points on day 7 because their intensity is just high enough to be detected and that in general their intensity is lower.

For the second injection event, shown in green, the mean brightness of the detected second oval points decreases through consecutive observations. The next observation is only 0.8 day after the injection event, and the mean brightness of the second oval points is 164 kR. This falls to 140 kR on the first orbit of day 13 and to 103 kR at the end of day 13. The only observation after the third injection event (blue) has second oval points with a mean brightness of 146 kR.

The automated detection does not distinguish between small injections (e.g., day 11), second oval “arcs,” e.g., (days 5, 6, and 7), and more complete second ovals (e.g., days 13 and 16). More points are expected to be detected for a longitudinally spread signature, such as an arc, compared to a small localized injection signature. The points detected at 0.8 day (in Figure 7b) correspond to the second observation of day 11 in which the HST images shows there are two small injections. This may explain why there is not such a large

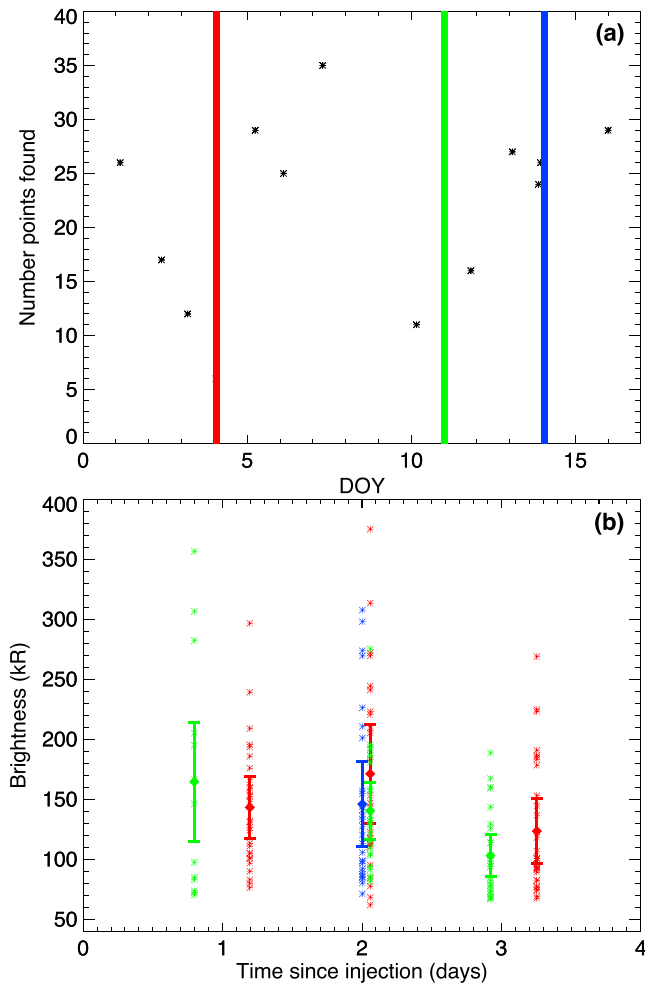


Figure 7. (a) Time series of the number of second oval points found in each observation normalized to the number of points that fit the detection criteria. The colored bars represent large injection events on days 4 (red), 11 (green), and 14 (blue). (b) The brightness of second oval points detected after injection observations. The mean brightness and standard deviation are overplotted for each observation.

increase in the number of second oval points detected for this observation Figure 7a, yet the peak brightness of the points is still high, at 356 kR (Figure 7b).

The two observations showing “full” second oval morphologies on days 13 and 16 occur ~ 2 days after large injections. Examination of Figure 7b shows that there does not appear to be a significant increase in brightness between the two observations despite the large injection event between them; day 13 shows points with a mean brightness of 140 kR ($t \sim 2$ days, green), and for day 16 ($t \sim 2$ days, blue) this is 146 kR. Figure 7a shows that a similar number of second oval points are detected on both images (days ~12 and ~16, respectively). This suggests that there is no cumulative effect of brightening due to two injection events occurring quickly after each other.

4.4. Temporal Evolution

Dumont et al. [2015] have shown in simulations that small injections of plasma in the inner magnetosphere are subcorotating. The localized injection signatures may be generated by electron scattering due to pitch angle diffusion and whistler mode waves. This corresponds to a subcorotating source for the second oval feature, so subcorotation of the feature may be expected.

Figure 1 (top) shows the development of second oval arcs from day 6 to day 7 in response to the injection event on day 4. The 150 kR brightness contour (pixels at greater than 150 kR) of the right arc (Figure 1b around 180° longitude) moves to higher longitudes (Figure 1c around 190° longitude), which corresponds to a subcorotating source. Both ends of the contour move 11°. The time between observations on day 6 and 7

is 28 h. Assuming that these are the same feature and that all movement is in the subcorotation direction, this gives a drift rate of 0.4°/h (98% corotation). Subcorotation was not explicitly seen in other sequences; however, this could be because the features were not bright enough to track.

The location of the main emission also changed through the campaign, possibly in response to the injection events. In order to determine the inner boundary for second oval points detection, the average main emission is expanded sequentially to best fit the main emission points detected. This gives a measure of the main emission position per HST observation. Between day 6 and day 16, there is an expansion of $\sim 0.5^\circ$. This is in agreement with the findings of *Badman et al.* [2016], who reported the main emission expanded 1° over the full 2014 campaign (day 1 to day 16).

4.5. Spectral Observations

Spectral observations of the auroral H_2 color ratio and brightness allow determination of the precipitating electron flux and energy. Spatially resolved spectral observations were taken consecutive with the HST images, in the wavelength range 110–170 nm. The color ratio is the ratio of H_2 emission intensity at 155–162 nm (which is unabsorbed by hydrocarbons) compared to 123–130 nm (absorbed by hydrocarbons). Applying a model of the atmosphere allows the depth of penetration of electrons to be calculated, thus giving a measure of the precipitating electron energy. Electron flux is determined from the auroral brightness using the approximation that $10 \text{ kR} \sim 1 \text{ mWm}^{-2}$ of input electron flux. For full details, see *Tao et al.* [2016] and *Gustin et al.* [2004].

The electron energy and electron flux may be different for the injection and second oval features. Spectral observations of a large injection signature are available on day 11 and of the second oval feature on day 16 of the campaign. Figures 8a and 8b show the location of the slit across the images for both days. On day 11, the slit passes through a large injection signature at low latitudes. On day 16, the slit passes through the dim main emission and second oval—the second oval appears as the lower latitude component.

Figure 8c and d show the energy flux-precipitating energy relationship for the “low latitude” feature spectral slit observations of days 11 and 16. The points corresponding to the large injection signature (Figures 8a and 8c) have a lower precipitating energy and higher-energy flux than the low latitude points from day 16 (Figures 8b and 8d). The second oval feature may have more higher-energy precipitating electrons than the large injection signature. The lines represent the energy and energy flux relation for different density electron sources being driven by field-aligned currents (i.e., the Knight relation). This may imply that the large injection signature is generated by field-aligned currents at its edges due to pressure gradients (e.g., the “bubble mode” [*Nakamura et al.*, 2001]), as well as some scattered electrons at high-energy and low-energy flux. The second oval signature could be formed by scattered electrons at a range of energies and low-energy flux.

5. Possible Generation Mechanism: Wave-Particle Interactions

We will consider both whistler mode waves and shear Alfvén waves as candidate waves for scattering or accelerating electrons into the loss cone to form the second oval feature. Generation of a longitudinally spread auroral signature requires scattered electrons from a longitudinally extended region, so it might be expected that precipitating electrons have drifted around the planet. Based on the enhancement of the second oval identified from Figure 7 following injection signatures, we now consider the possible effect of a localized injection in the region $7-20 R_J$. Injected electrons are expected to drift opposite to the corotation direction as a result of the gradient and curvature of the magnetic field. Dispersion is also expected according to the energies of the electrons [*Mauk et al.*, 2002]. A dipole magnetic field is assumed. For electrons, the drift velocity can be approximated as [*Mauk et al.*, 1999]

$$\omega = 6.92 \times 10^{-7} \frac{q_0}{q} TLH \quad (1)$$

where $H = 0.7 + 0.3 \sin \alpha$, a numerically solved correction factor to the drift velocity, $T = E \frac{E+2E_{0m}}{E+E_{0m}}$, the electron temperature, ω is the drift velocity of the electrons in rad/s, q is the charge, q_0 is the proton charge, L is the L shell number, α is the equatorial pitch angle in radians, E_{0m} is the rest mass, and E is the energy in MeV. *Mauk et al.* [1997, 1999] report typical electron energies in the range $\sim 10-1000$ keV observed in this region using EPD measurements from Galileo. Over this energy range, between $L = 10-20$ with equatorial pitch angles

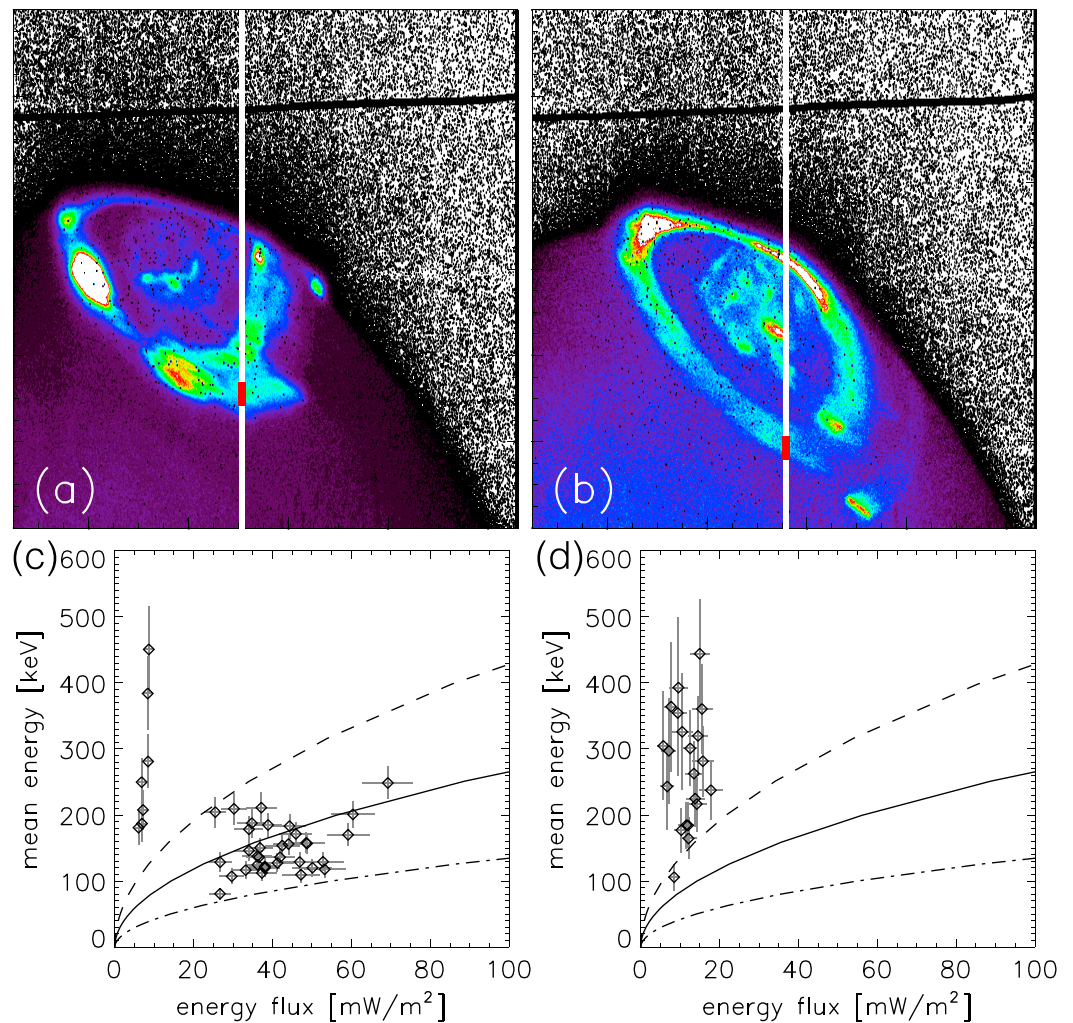


Figure 8. HST unprojected images of (a) day 11, injection signatures, and (b) day 16, second oval, showing slit intersection (white) over the images taken before spectral observation; the red line indicates the low-latitude region of interest. The low-latitude region on day 11 is interpreted as a large injection signature. On day 16, the low-latitude region contains the main emission and second oval feature—the lowest latitude portion could be the second oval. (bottom) Electron energy and energy flux for (c) day 11 and (d) day 16 for the low latitude points only. The expected relation between the mean energy and energy flux according to the Knight relation is shown for different source populations, $N_0 = 0.0026 \text{ cm}^{-3}$ (solid), $N_0 = 0.001 \text{ cm}^{-3}$ (dashed), and $N_0 = 0.01 \text{ cm}^{-3}$ (dash dotted). The main emission is expected to obey the relation described by these lines [Gustin et al., 2016].

between 10 and 90°, equation (1) yields the range of 4–705 days (with higher-energy electrons at larger pitch angles and at further L shells taking a shorter time) to spread 360° in longitude; this corresponds to a drift rate of 0.02–3.82°/h. This corresponds to a 89–99% corotation rate, which encompasses the rate found from the HST images.

Plasma wave growth may occur as a result of the temperature anisotropy across the injection. *Katoh et al.* [2011] have shown that at Jupiter, whistler mode chorus enhancements may be efficiently generated by energetic electron populations. Waves have been reported in the region of interest [e.g., *Radioti et al.*, 2009; *Tomás et al.*, 2004a, 2004b; *Menietti et al.*, 2016]. Although studies at Earth have shown wave growth is expected to be rapid (few hours, e.g., *Thorne et al.*, 2010), waves are not typically seen in all locations at all times—the growth process may be throttled by the surrounding cold plasma conditions, such as its density [*Li et al.*, 2009a, 2009b]. The efficiency of the wave-particle scattering mechanism is affected by many parameters including the particle energy, wave frequency, and the cold plasma density [e.g., *Glauert and Horne*, 2005]. The range of electron energies from the injections in this region typically interacts strongly with the frequency of chorus waves observed here [*Woodfield et al.*, 2014].

Should good wave growth and resonance conditions be achieved, the electron is expected to be scattered into the loss cone. There may be multiple injections, or multiple parts of the same injection with different dominant energies. The auroral feature may therefore appear patchy and in discontinuous arcs. This process has been reported at Earth [e.g., *Thorne et al.*, 2010; *Ni et al.*, 2011; *Tao et al.*, 2011], where injected plasma sheet electrons have been seen to enhance the diffuse auroral oval via pitch angle scattering due to chorus waves.

Shear Alfvén waves, which accelerate electrons through generated parallel electric fields, may also be responsible for the auroral precipitation observed. Parallel propagating Alfvén wave generation is expected where there is a change in magnetic topology, for example, at reconnection events [*Shay et al.*, 2011] and the boundary of hot plasma injections. Magnetospheric shear Alfvén waves have been observed to contribute to the generation of aurora at Earth, particularly along field lines associated with the plasma sheet boundary layer [*Wygant et al.*, 2000; *Watt and Rankin*, 2010, 2012].

The auroral signatures of shear Alfvén wave-driven electron precipitation tends to be latitudinally constrained since they accelerate electrons parallel to the field lines upon which they act. The field lines can map to a large region in the magnetosphere. It is feasible, therefore, that this process could be responsible for the latitudinally constrained signature reported here. Additionally, the spectra associated with the second oval may show high mean energy electrons, as expected for Alfvén waves.

6. Interpretation and Discussion

Arcs of emission equatorward of the main emission have been detected in Jupiter's aurora. Figure 7a shows that this feature is brighter across more longitudes after large injections. The second oval feature can appear in arcs (see HST images from day 4 to day 7 in Figure 1a), which extend to higher longitudes with time, as expected for a source that is subcorotating. The rate of subcorotation for the second oval estimated from the HST images ($0.4^\circ/\text{h}$) is in agreement with the theoretical drift rate calculated for electrons with energy around 400–800 keV at L shells of 10–20 at equatorial pitch angle 60° .

Magnetic mapping of the injection signatures from HST images on day 11 and of the average position of the second emission show that the sources of these two features overlap in the equatorial plane. Figure 5c shows the mapped position of the second oval feature lies around $\sim 9\text{--}13 R_J$, where the field lines are roughly dipolar. The second oval lies close to the Ganymede footprint contour. The location found here is close to that found in previous work [*Tomás et al.*, 2004b]. The second oval location found in this work and previous work are in agreement with a source around $10\text{--}17 R_J$, where the PAD boundary is thought to lie. The location of the second oval feature, its increased brightness 1–3 days following injections, and apparent subcorotation suggests that the auroral second oval feature can be enhanced as a result of an evolution of the injected plasma. Injected plasma has a latitudinally broad signature, but particles which have drifted longitudinally may be scattered by waves produce a longitudinally spread but latitudinally confined signature.

Spectral studies of auroral signatures allow the energies and fluxes of precipitating electrons to be determined. Figure 8 compares the injected plasma and second oval feature and shows that the second oval feature tends to be formed by higher-energy electrons with lower fluxes than the injected plasma signature. It is suggested that the electrons may have been energized and scattered as part of wave-particle interactions for both the initial injection signatures and the second oval feature. *Tomás et al.* [2004b] predicted that for electrons in the two EPD energy channels 55–188 and 55–304 keV, the precipitating flux may be 36–115 kR to 59–276 kR, respectively. This is in agreement with the range of brightnesses found for second oval points in Figure 6. Figure 8d shows the mean electron energy for the scattered electrons forming the second oval may extend up to ~ 500 keV; more energetic electrons may drive brighter aurora (up to a few hundred keV, above which UV absorption by hydrocarbons at lower altitudes throttles the auroral brightness [*Tao et al.*, 2011]). The higher-energy electrons could therefore account for the higher end tail of the brightness distribution of the feature, as shown in Figure 6.

Figure 4 compares second oval points detected in arcs on day 6 and the more full morphology seen on day 16 and shows that the arcs may be visible parts of the more complete oval feature. Wave growth and resonance processes are affected by cold plasma conditions and therefore do not necessarily occur at equal rates at all local times. Brighter arcs could be generated by wave-particle excitation processes where the cold plasma density surrounding the initial injected plasma is appropriate for wave growth and resonance. Figure 7b shows superposed epoch analysis of the second oval brightness. The brightness tends to increase between 1 and

2 days after the injection event and fades thereafter. This suggests wave growth and resonance processes that scatter electrons into the ionosphere can be a long-lived (at least 3 days) process at Jupiter.

Three large injections of hot plasma are observed in this campaign in quick succession. Figure 7a shows that there is a slightly higher number of second oval points detected on day 16 after the day 14 injection event, showing that the feature spreads to more longitudes. Figure 7b shows that the peak brightness of the feature increases by ~ 100 kR after the day 14 injection event. The mean brightness remains constant. It is suggested that wave-particle interactions are sustained by the successive large injections.

Previous work has suggested that the second oval is the auroral counterpart of a step down in plasma angular velocity mapping to the main oval [Hill, 2001; Cowley and Bunce, 2001; Vogt *et al.*, 2011]. It is noted this is not reflected in empirical models of corotation breakdown [Grodent *et al.*, 2003]. Enhancements of the second oval as studied here would be related to a step in corotation breakdown closer to the planet, but not an inward shift of the main emission source (since its auroral signatures remains). However, Figures 8c and 8d show that the mean energy versus energy flux relation for the second oval is different to the main emission curves (which obey the Knight relation) shown by Gustin *et al.* [2016].

7. Summary

We have identified a UV auroral arc feature of varying longitudinal extent equatorward of the main emission. The location of the second oval feature lies between the Ganymede and Europa moon footprint contours between 150 and 240° system III longitude, corresponding to a source in the inner magnetosphere between ~ 9 – $13 R_J$. This is in the same region of 10 – $17 R_J$ known as the PAD boundary, where electrons have been observed to be scattered into a field-aligned configuration and cause auroral precipitation. The feature is enhanced in both brightness and longitudinal spread 1–3 days after large injections signatures. Spectral analysis of the H_2 emissions shows that the precipitating electrons have a higher-energy and lower flux than the electrons generating large injection signatures.

We suggest that wave-particle interactions are responsible for the scattering of electrons in this region. We also suggest that the plasma injections can act as a temperature anisotropy and particle source to enhance wave intensity and subsequent electron scattering into the ionosphere. We suggest this process can last up to at least 3 days. Changes to the magnetic field topology around an injection may also generate shear Alfvén waves and therefore accelerate electrons parallel to the magnetic field resulting in precipitation.

Acknowledgments

R.L.G. was supported by a STFC studentship. S.V.B. was supported by an STFC fellowship (ST/M005534/1). E.E.W. is supported by an STFC grant (ST/M00130X/1). This work was partly supported by JSPS KAKENHI grant 15K17769. We acknowledge support from the International Space Science Institute (ISSI) since this work was discussed at a meeting of the 'Influence of Io on Jupiter's magnetosphere' team. This work is based on observations made with the NASA/ESA Hubble Space Telescope (observation ID: GO13035), obtained at the Space Telescope Science Institute (STScI), which is operated by AURA, Inc., for NASA. The Hubble observations are available from the STScI website.

References

- Badman, S. V., *et al.* (2016), Weakening of Jupiter's main auroral emission during January 2014, *Geophys. Res. Lett.*, *43*, 988–997, doi:10.1002/2015GL067366.
- Bhattacharya, B., R. M. Thorne, and D. J. Williams (2001), On the energy source for diffuse Jovian auroral emissivity, *Geophys. Res. Lett.*, *28*(14), 2751–2754, doi:10.1029/2000GL012616.
- Bonfond, B. (2012), When Moons create aurora: The satellite footprints on giant planets, in *Auroral Phenomenology and Magnetospheric Processes: Earth And Other Planets*, Geophysical Monograph Series, vol. 197, edited by A. Keilling *et al.*, pp. 133–140, AGU, Washington, D. C., doi:10.1029/2011GM001169.
- Bonfond, B., D. Grodent, J.-C. Gérard, T. Stallard, J. T. Clarke, M. Yoneda, A. Radioti, and J. Gustin (2012), Auroral evidence of Io's control over the magnetosphere of Jupiter, *Geophys. Res. Lett.*, *39*, L01105, doi:10.1029/2011GL050253.
- Clarke, J. T., *et al.* (2009), Response of Jupiter's and Saturn's auroral activity to the solar wind, *J. Geophys. Res.*, *114*, A05210, doi:10.1029/2008JA013694.
- Connerney, J. E. P., M. H. Acuña, and N. F. Ness (1981), Modeling the Jovian current sheet and inner magnetosphere, *J. Geophys. Res.*, *86*(A10), 8370–8384, doi:10.1029/JA086iA10p08370.
- Cowley, S. W. H., and E. J. Bunce (2001), Origin of the main auroral oval in Jupiter's coupled magnetosphere-ionosphere system, *Planet. Space Sci.*, *49*, 1067–1088, doi:10.1016/S0032-0633(00)00167-7.
- Dumont, M., D. Grodent, A. Radioti, and J.-C. Gérard (2014), Jupiter's equatorward auroral features: Possible signatures of magnetospheric injections, *J. Geophys. Res. Space Physics*, *119*, 10,068–10,077, doi:10.1002/2014JA020527.
- Dumont, M., D. Grodent, A. Radioti, B. Bonfond, E. Roussos, and C. Paranicas (2015), *Simulations of the Auroral Signatures of Jupiter's Magnetospheric Injections*, 10 EPSC2015-642, EPSC Abstracts, Nantes, France.
- Fujimoto, M., and A. Nishida (1990), Monte Carlo simulation of energization of Jovian trapped electrons by recirculation, *J. Geophys. Res.*, *95*, 3841–3853, doi:10.1029/JA095iA04p03841.
- Glauert, S. A., and R. B. Horne (2005), Calculation of pitch angle and energy diffusion coefficients with the PADIE code, *J. Geophys. Res.*, *110*, A04206, doi:10.1029/2004JA010851.
- Gray, R. L., S. V. Badman, B. Bonfond, T. Kimura, H. Misawa, J. D. Nichols, M. F. Vogt, and L. C. Ray (2016), Auroral evidence of radial transport at Jupiter during January 2014, *J. Geophys. Res. Space Physics*, *121*, 9972–9984, doi:10.1002/2016JA023007.
- Grodent, D., J. T. Clarke, J. Kim, J. H. Waite, and S. W. H. Cowley (2003), Jupiter's main auroral oval observed with HST-STIS, *J. Geophys. Res.*, *108*(A11), 1389, doi:10.1029/2003JA009921.
- Gustin, J., J.-C. Gérard, D. Grodent, S. W. H. Cowley, J. T. Clarke, and A. Gward (2004), Energy-flux relationship in the FUV Jovian aurora deduced from HST-STIS spectral observations, *J. Geophys. Res.*, *109*, A10205, doi:10.1029/2003JA010365.

- Gustin, J., B. Bonfond, D. Grodent, and J.-C. Gérard (2012), Conversion from HST ACS and STIS auroral counts into brightness, precipitated power, and radiated power for H₂ giant planets, *J. Geophys. Res.*, *117*, A07316, doi:10.1029/2012JA017607.
- Gustin, J., D. Grodent, L. Ray, B. Bonfond, E. Bunce, J. Nichols, and N. Ozak (2016), Characteristics of north Jovian aurora from STIS FUV spectral images, *Icarus*, *268*, 215–241, doi:10.1016/j.icarus.2015.12.048.
- Hess, S. L. G., B. Bonfond, P. Zarka, and D. Grodent (2011), Model of the Jovian magnetic field topology constrained by the Io auroral emissions, *J. Geophys. Res.*, *116*, A05217, doi:10.1029/2010JA016262.
- Hill, T. W. (2001), The Jovian auroral oval, *J. Geophys. Res.*, *106*, 8101–8108, doi:10.1029/2000JA000302.
- Katoh, Y., F. Tsuchiya, Y. Miyoshi, A. Morioka, H. Misawa, R. Ujii, W. S. Kurth, A. T. Tomás, and N. Krupp (2011), Whistler mode chorus enhancements in association with energetic electron signatures in the Jovian magnetosphere, *J. Geophys. Res.*, *116*, A02215, doi:10.1029/2010JA016183.
- Kimura, T., et al. (2015), Transient internally-driven aurora at Jupiter discovered by Hisaki and the Hubble Space Telescope, *Geophys. Res. Lett.*, *42*, 1662–1668, doi:10.1002/2015GL063272.
- Kivelson, M. G., K. K. Khurana, C. T. Russell, and R. J. Walker (1997), Intermittent short-duration magnetic field anomalies in the Io torus: Evidence for plasma interchange?, *Geophys. Res. Lett.*, *24*, 2127, doi:10.1029/97GL02202.
- Li, W., R. M. Thorne, V. Angelopoulos, J. W. Bonnell, J. P. McFadden, C. W. Carlson, O. LeContel, A. Roux, K. H. Glassmeier, and H. U. Auster (2009a), Evaluation of whistler-mode chorus intensification on the nightside during an injection event observed on the THEMIS spacecraft, *J. Geophys. Res.*, *114*, A00C14, doi:10.1029/2008JA013554.
- Li, W., R. M. Thorne, V. Angelopoulos, J. Bortnik, C. M. Cully, B. Ni, O. LeContel, A. Roux, U. Auster, and W. Magnes (2009b), Global distribution of whistler-mode chorus waves observed on the THEMIS spacecraft, *Geophys. Res. Lett.*, *36*, L09104, doi:10.1029/2009GL037595.
- Louarn, P., C. P. Paranicas, and W. S. Kurth (2014), Global magnetodisk disturbances and energetic particle injections at Jupiter, *J. Geophys. Res. Space Physics*, *119*, 4495–4511, doi:10.1002/2014JA019846.
- Mauk, B. H., D. J. Williams, and R. W. McEntire (1997), Energy-time dispersed charged particle signatures of dynamic injections in Jupiter's inner magnetosphere, *Geophys. Res. Lett.*, *24*(23), 2949–2952, doi:10.1029/97GL03026.
- Mauk, B. H., D. J. Williams, R. W. McEntire, K. K. Khurana, and J. G. Roederer (1999), Storm-like dynamics of Jupiter's inner and middle magnetosphere, *J. Geophys. Res.*, *104*, 22,759–22,778, doi:10.1029/1999JA900097.
- Mauk, B. H., J. T. Clarke, D. Grodent, J. H. Waite, C. P. Paranicas, and D. J. Williams (2002), Transient aurora on Jupiter from injections of magnetospheric electrons, *Nature*, *415*, 1003–1005.
- Menietti, J. D., J. B. Groene, T. F. Averkamp, R. B. Horne, E. E. Woodfield, Y. Y. Shprits, M. de Soria-Santacruz Pich, and D. A. Gurnett (2016), Survey of whistler mode chorus intensity at Jupiter, *J. Geophys. Res. Space Physics*, *121*, 9758–9770, doi:10.1002/2016JA022969.
- Nakamura, R., W. Baumjohann, R. Schödel, M. Brittnacher, V. A. Sergeev, M. Kubyshkina, T. Mukai, and K. Liou (2001), Earthward flow bursts, auroral streamers, and small expansions, *J. Geophys. Res.*, *106*, 10,791–10,802, doi:10.1029/2000JA000306.
- Ni, B., R. M. Thorne, N. P. Meredith, R. B. Horne, and Y. Y. Shprits (2011), Resonant scattering of plasma sheet electrons leading to diffuse auroral precipitation: 2. Evaluation for whistler mode chorus waves, *J. Geophys. Res.*, *116*, A04219, doi:10.1029/2010JA016233.
- Nichols, J. D., J. T. Clarke, J. C. Gérard, D. Grodent, and K. C. Hansen (2009), Variation of different components of Jupiter's auroral emission, *J. Geophys. Res.*, *114*, A06210, doi:10.1029/2009JA014051.
- Nishida, A. (1976), Outward diffusion of energetic particles from the Jovian radiation belt, *J. Geophys. Res.*, *81*(10), 1771–1773, doi:10.1029/JA081i010p01771.
- Radioti, A., A. T. Tomás, D. Grodent, J.-C. Gérard, J. Gustin, B. Bonfond, N. Krupp, J. Woch, and J. D. Menietti (2009), Equatorward diffuse auroral emissions at Jupiter: Simultaneous HST and Galileo observations, *Geophys. Res. Lett.*, *36*, L07101, doi:10.1029/2009GL037857.
- Radioti, A., E. Roussos, D. Grodent, J.-C. Gérard, N. Krupp, D. G. Mitchell, J. Gustin, B. Bonfond, and W. Pryor (2013), Signatures of magnetospheric injections in Saturn's aurora, *J. Geophys. Res. Space Physics*, *118*, 1922–1933, doi:10.1002/jgra.50161.
- Santolík, O., D. A. Gurnett, G. H. Jones, P. Schippers, F. J. Cray, J. S. Leisner, G. B. Hospodarsky, W. S. Kurth, C. T. Russell, and M. K. Dougherty (2011), Intense plasma wave emissions associated with Saturn's moon Rhea, *Geophys. Res. Lett.*, *38*, L19204, doi:10.1029/2011GL049219.
- Shay, M. A., J. F. Drake, J. P. Eastwood, and T. D. Phan (2011), Super-Alfvénic propagation of substorm reconnection signatures and poynting flux, *Phys. Rev. Lett.*, *107*, 065001, doi:10.1103/PhysRevLett.107.065001.
- Tao, C., S. V. Badman, and M. Fujimoto (2011), UV and IR auroral emission model for the outer planets: Jupiter and Saturn comparison, *Icarus*, *213*, 581–592, doi:10.1016/j.icarus.2011.04.001.
- Tao, C., et al. (2016), Variation of Jupiter's aurora observed by Hisaki/EXCEED: 1. Observed characteristics of the auroral electron energies compared with observations performed using HST/STIS, *J. Geophys. Res. Space Physics*, *121*, 4041–4054, doi:10.1002/2015JA021271.
- Tao, X., R. M. Thorne, W. Li, B. Ni, N. P. Meredith, and R. B. Horne (2011), Evolution of electron pitch angle distributions following injection from the plasma sheet, *J. Geophys. Res.*, *116*, A04229, doi:10.1029/2010JA016245.
- Thorne, R. M., T. P. Armstrong, S. Stone, D. J. Williams, R. W. McEntire, S. J. Bolton, D. A. Gurnett, and M. G. Kivelson (1997), Galileo evidence for rapid interchange transport in the Io torus, *Geophys. Res. Lett.*, *24*, 2131, doi:10.1029/97GL01788.
- Thorne, R. M., B. Ni, X. Tao, R. B. Horne, and N. P. Meredith (2010), Scattering by chorus waves as the dominant cause of diffuse auroral precipitation, *Nature*, *467*(7318), 943–946.
- Tomás, A., J. Woch, N. Krupp, A. Lagg, K.-H. Glassmeier, M. K. Dougherty, and P. G. Hanlon (2004a), Changes of the energetic particles characteristics in the inner part of the Jovian magnetosphere: A topological study, *Planet. Space Sci.*, *52*, 491–498, doi:10.1016/j.pss.2003.06.011.
- Tomás, A. T., J. Woch, N. Krupp, A. Lagg, K.-H. Glassmeier, and W. S. Kurth (2004b), Energetic electrons in the inner part of the Jovian magnetosphere and their relation to auroral emissions, *J. Geophys. Res.*, *109*, A06203, doi:10.1029/2004JA010405.
- Tomás, A. T. M. (2005), Energetic particles in the Jovian magnetosphere and their relation to auroral emissions, PhD Thesis, Braunschweig Univ. of Technol.
- Vasavada, A. R., A. H. Bouchez, A. P. Ingersoll, B. Little, C. D. Anger, and G. S. Team (1999), Jupiter's visible aurora and Io footprint, *J. Geophys. Res.*, *104*, 27,133–27,142, doi:10.1029/1999JE001055.
- Vogt, M. F., M. G. Kivelson, K. K. Khurana, R. J. Walker, B. Bonfond, D. Grodent, and A. Radioti (2011), Improved mapping of Jupiter's auroral features to magnetospheric sources, *J. Geophys. Res.*, *116*, A03220, doi:10.1029/2010JA016148.
- Watt, C., and R. Rankin (2012), Alfvén wave acceleration of auroral electrons in warm magnetospheric plasma, in *Auroral Phenomenology and Magnetospheric Processes: Earth and Other Planets*, edited by A. Keiling et al., pp. 251–260, AGU, Washington, D. C., doi:10.1029/2011GM001171.
- Watt, C. E. J., and R. Rankin (2010), Do magnetospheric shear Alfvén waves generate sufficient electron energy flux to power the aurora?, *J. Geophys. Res. Space Physics*, *115*, A07224, doi:10.1029/2009JA015185.
- Woodfield, E., R. Horne, S. Glauert, J. Menietti, and Y. Shprits (2014), The origin of Jupiter's outer radiation belt, *J. Geophys. Res. Space Physics*, *119*, 3490–3502, doi:10.1002/2014JA019891.

- Wygant, J., et al. (2000), Polar spacecraft based comparisons of intense electric fields and poynting flux near and within the plasma sheet-tail lobe boundary to UVI images: An energy source for the aurora, *J. Geophys. Res.*, *105*, 18,675–18,692.
- Xiao, F., R. M. Thorne, D. A. Gurnett, and D. J. Williams (2003), Whistler-mode excitation and electron scattering during an interchange event near Io, *Geophys. Res. Lett.*, *30*(14), 1749, doi:10.1029/2003GL017123.